OEA | Opto-Electronic Advances

Article

April 2026, Vol. 9, No. 4

Open Access

Polarization-guided diffusion prior for eyeglass reflection removal

Yating Chen and Liangcai Cao*

Abstract: In video conferencing and facial recognition applications, eyeglass reflection often obscures critical facial features. Polarization information helps disentangle reflection and transmission components. Existing polarization reflection removal approaches rely on large-scale paired polarization datasets, making them hard to generalize to the scenes under unseen lighting conditions. To address these challenges, we propose PDPrior, an untrained polarization-guided diffusion prior for eyeglass reflection removal. The PDPrior requires no training data, and no ground-truth reflection-free images. It operates solely on polarization observations collected at test time to achieve artifact-free, high-fidelity reflection removal. The PDPrior leverages the generative prior of a diffusion model and introduces polarization as guidance to control the generation process. The self-supervised loss based on the forward model is employed to alternately update the reflection and transmission variables, endowing the generative model with physical interpretability. Extensive experimental results validate the effectiveness and robustness of the method on eyeglass reflection data captured in both indoor and outdoor lighting conditions, achieving higher face image quality assessment scores for recognition performance compared to state-of-the-art methods.

Keywords: eyeglass reflection removal; diffusion model; untrained learning; polarization-guided optimization

DOI: 10.29026/oea.2026.250249 | CSTR: 32247.14.oea.2026.250249

Citation: Chen YT, Cao LC. Polarization-guided diffusion prior for eyeglass reflection removal. *Opto-Electron Adv* **9**, 250249 (2026).

1 Introduction

With the rapid development of network communication technologies and the advent of the 5G era, breakthroughs have been achieved in high-definition video encoding/decoding and real-time mobile video transmission. As a result, global online interactions have witnessed exponential growth. Against this backdrop, the video conferencing market has experienced explosive expansion, with major international platforms such as Zoom, Microsoft Teams, Tencent Meeting and Feishu, emerging and evolving rapidly. Meanwhile, driven by advances in deep learning algorithms, facial recognition-based biometric authentication has become a mainstream identity verification method in key domains such as government and finance services, owing to its convenience and security. However, in scenarios such as video conferencing and facial recognition, eyeglass reflection often leads to significant occlusion of facial features. In video conferencing, such reflection degrades visual perception and distracts online participants. In facial recognition, reflection regions interfere with facial localization, increasing the recognition errors.

Eyeglass reflection typically involves either specular highlights or ambient scene reflections, or a combination of both. The captured image with reflection can be regarded as a superposition of a transmission layer and a reflection layer. The objective of reflection removal is to effectively separate these two components. Currently, reflection removal methods can be broadly categorized into single-image-based and multi-image-based approaches, depending on the input modality. Multi-image-based methods utilize either flash image sequences or polarization image sequences to facilitate reflection removal. Single-image-based methods lack sufficient cues, such as temporal, angular, or polarization information, to distinguish between the reflection and transmission layers, and thus typically rely on modeling the statistical characteristics. For instance, some approaches have exploited the higher blur level and weaker gradient magnitude of the reflection layer to identify reflection regions and reconstruct the transmission content using a

Received: 17 September 2025

Accepted: 9 January 2026

Published online: 9 March 2026

State Key Laboratory of Precision Measurement Technology and Instruments, Department of Precision Instruments, Tsinghua University, Beijing 100084, China.

*Correspondence: LC Cao, E-mail: clc@tsinghua.edu.cn

non-local self-similarity sparse prior and a gradient sparsity constraint[1,2]. Similarly, Yang Y et al.[3] proposed to leverage the blurry nature of reflection, removing reflection edges through gradient thresholding and solving the reflection-free image using convex optimization[4]. Several studies have approached the problem from the perspective of unwanted artifact removal and image restoration, aiming to achieve more general image reconstruction and quality enhancement, such as MB-TaylorFormer v2[5], GDP[6], MC-Blur[7], and DBLRNet[8]. Sandhan T et al.[9] focused on eyeglass reflection and integrated facial symmetry prior into a non-convex optimization scheme to achieve reflection removal by exploiting the sparsity of reflection gradient. Subsequent work has gradually shifted toward deep neural network-based solutions. Perceptual loss and exclusion loss were employed to train end-to-end networks[10], while other losses based on the characteristics of eyeglass reflection, such as eye-symmetry loss, were designed to avoid visual artifacts[11]. Li C et al.[12] integrated the iterative convex optimization process into deep networks via cascaded architecture to improve the reliability of blind separation. More recently, Huang JJ et al.[13] designed the Deep Exclusion Unfolding Network, focusing on minimizing the shared features between the transmission and reflection layers to enhance separation. However, these methods typically rely on paired reflection/reflection-free data for supervised training, which significantly hinder their scalability and applicability in real-world scenarios. To enable unsupervised single-image reflection removal, Deep Image Prior (DIP) was introduced[14,15]. Due to the semantic ambiguity between reflection and transmission layers, DIP-based methods often fail to achieve accurate separation. In the past three years, several studies have explored diffusion model, leveraging the generative diversity to reconstruct the missing transmission content in regions heavily occluded by reflection[16–18]. Yi ZL et al.[18] focused on eyeglass reflection scenes and proposed DL2G, which employs a pretrained degradation estimation module to detect reflective regions, followed by a local structure-aware diffusion model to recover fine-grained textures hidden under reflection.

Nonetheless, single-image reflection removal methods remain heavily reliant on strong scene assumptions, making it difficult to achieve both generality and fidelity under diverse real-world conditions. In contrast, multi-image-based approaches can capture diverse reflection characteristics under different illumination, angular, or polarization conditions, thereby addressing the ill-posed problem of separating transmission and reflection layers. One common strategy is to leverage illumination control. By capturing paired images under ambient lighting with and without the flash, and subtracting the two, one obtained a “flash-only” image that suppressed reflection[19,20]. Recently, Shi WQ et al.[21] proposed a deep-learning-based control system that dynamically adjusted a ring-shaped lighting system in four polarized directions to eliminate specular highlights for the Fourier light field microscopy system. However, such methods require integration of high-power illumination modules and the sensors, resulting in bulky systems with high energy consumption. In contrast, many thin, compact, and portable snapshot polarization imaging systems already exist, such as the commercialized Sony division-of-focal-plane polarization sensor and the emerging research focus on metasurface-based polarimetric imaging sensors[22,23]. Metasurfaces, due to their flexibility in multi-parameter modulation, are strong candidates for polarization manipulation[24]. In particular, dielectric metasurfaces can realize highly efficient polarization-dependent wavefront manipulation[25] and polarization multiplexing[26]. Favorable conditions are created for acquiring polarization information in real-world scenarios. Since both transmitted and reflected light can be partially polarized, polarization filtering has been explored to suppress reflection. Nevertheless, complete suppression only occurs under ideal conditions, such as when the incident angle matches the Brewster angle. As a result, physical polarizing filters cannot achieve complete extinction.

Consequently, data-driven polarization imaging technologies have gradually found applications in reflection removal[27]. Wen SJ et al.[28] constructed polarization chromaticity images from four polarization-direction intensity images to cluster pixels with similar diffuse colors, using the cluster result as a prior in iterative optimization for separating specular reflection. Wang X et al.[29] further optimized the network structure for polarization-guided reflection removal by proposing a dual-stream architecture with feature-attention guidance to estimate both the transmission and reflection layers. To construct paired polarization datasets, the synthetic pipeline was proposed to generate realistic reflection polarized data from curved surfaces and dynamic environments[30,31]. This work demonstrates the potential of integrating traditional polarization optics with differentiable computational imaging, offering an efficient pathway for reflection removal. However, there still exists the domain gap between synthetic data and real-world data distributions. A field-of-view-aligned polarization dataset covering over 100 types of glass materials was introduced, including reflection-free ground truth and corresponding images captured from four polarization angles, to improve real-world performance[32]. Most recently, PolaRGB[33] was released, a large-scale dataset of indoor and outdoor RGB and polarization images under diverse lighting conditions. In this work[33], the PolarFree leverages the diffusion process to generate reflection-free cues. However, currently available public polarization datasets do not include eyeglass reflection scenarios, limiting their effectiveness for eyeglass reflection removal.

In summary, existing optimization-based polarization reflection removal methods only work under strong assumptions and tend to degrade the details of the transmission scene. Deep learning-based approaches typically depend on paired polarization reflection images and

reflection-free ground truth, which poses significant challenges in data acquisition and generalization. To address these challenges, we propose an untrained method: PDPrior (polarization-guided diffusion prior for eyeglass reflection removal). Figure 1 illustrates the results of PDPrior and highlights its advantages and uniqueness compared with existing approaches. The PDPrior operates solely on polarized observations acquired at test time, free of pretrained models, training data, and ground-truth reflection-free images. The DIP, as an untrained method[14,34], requires thousands of iterations to update network parameters. Unlike DIP, the proposed PDPrior keeps the network parameters frozen during the optimization process and only updates the network input. This design significantly reduces the number of iterations while maintaining performance, leading to approximately two orders of magnitude improvement in inference speed. The PDPrior leverages the generative prior of a diffusion model and introduces polarization information as guidance to control the generation process. During each sampling step, the reflection and transmission variables are alternately and iteratively updated via gradient descent. Specifically, a division-of-focal-plane polarization camera is used to capture intensity images at 0°, 45°, 90°, and 135° polarization angles. The reflection diffusion model takes the unpolarized intensity image as input. The degree of linear polarization (DoLP) is then used to preliminarily identify reflection regions and the diffusion prior of progressively darkening facial content during generation process, which enables the model to focus on reflective regions. The optimal polarization-direction image with minimal reflection is adaptively selected as input to the transmission diffusion model based on intensity, gradient, and entropy constraints. The transmission diffusion model uses the DoLP to compute the transmission coefficient. The generation of transmission image is guided by the forward model of reflection formation, ensuring physical interpretability. To our knowledge, this is the first work to apply untrained diffusion model to the task of polarized reflection removal, marking a novel and promising direction in the field. We validate PDPrior on our polarization eyeglass reflection datasets under various indoor and outdoor lighting conditions. Experimental results show that PDPrior achieves artifact-free, high-fidelity reflection removal, and outperforming state-of-the-art methods. Moreover, the PDPrior consistently obtains higher and more robust scores in face image quality assessments for recognition performance.

2 Methods

Eyeglass reflection typically exhibits image characteristics distinct from background transmission, and these differences can be exploited for reflection removal. However, such characteristics are sensitive to illumination and difficult to unify into a general representation. To address this issue, we leverage the flexible generative capability of generative model to reconstruct reflection-free transmission images. Nevertheless, without proper constraints, generative model may produce results that deviate from physical reality, making effective guidance a critical challenge. As one of the three fundamental properties of light, along with color and intensity[35], polarization can effectively distinguish reflection regions. By incorporating polarization information, the PDPrior achieves reflection and transmission image generation without requiring training data, ensuring the physical reliability of the generated results.

2.1 Principle of polarization reflection suppression

Based on the physical principles of reflection and transmission in a dual-layer glass medium, the reflection and

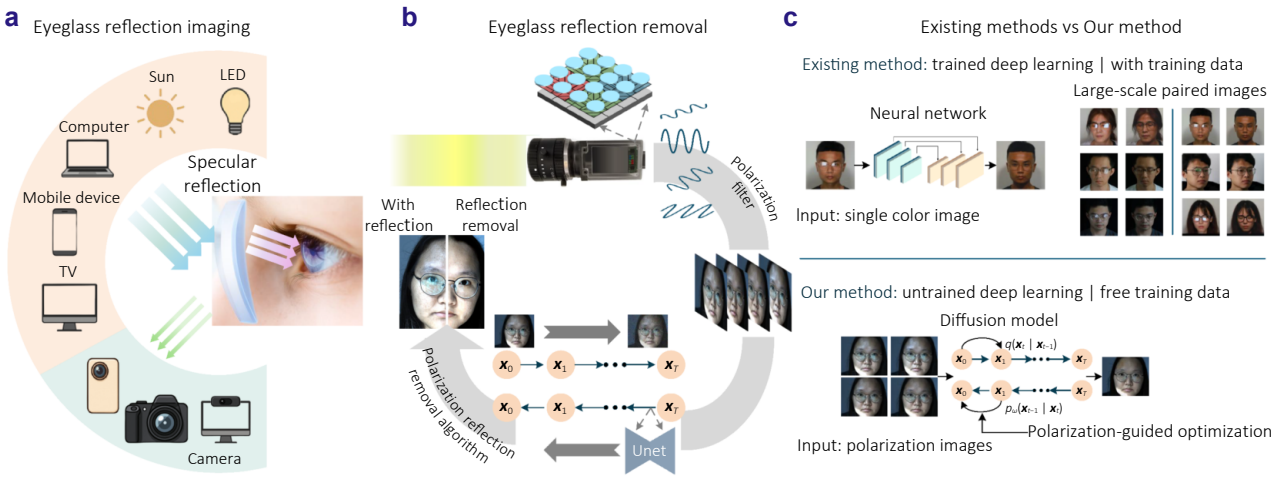


Fig. 1 | Concept of PDPrior for eyeglass reflection removal. (a) Schematic diagram of eyeglass reflection removal for the PDPrior. (b) Results before and after eyeglass reflection removal using the PDPrior. (c) Comparison between existing eyeglass reflection removal methods and the PDPrior. The paired dataset is sourced from the real-world eyeglass reflection (ReyeR) dataset[11].

transmission properties can be modeled by the following equation[36]:

$$\boldsymbol{I}(x)=\boldsymbol{A}(x)\,\boldsymbol{I}_{\mathrm{B}}(x)+(1-\boldsymbol{A}(x))\,\boldsymbol{I}_{\mathrm{R}}(x)\ , \tag{1}$$

where the transmission image $\boldsymbol{I}_{\mathrm{B}}$ refers to the facial light intensity originating from behind the eyeglass, while the reflection image $\boldsymbol{I}_{\mathrm{R}}$ represents either strong specular highlights or ambient scene reflections projected onto the eyeglass. According to Snell's law, this imaging model describes a process of multiple refractions and reflections occurring within the double-surfaced transparent planar medium[31]. The transmission coefficient $\boldsymbol{A}$ is influenced by several factors, including the refractive index of the glass, the angle of light incidence, and light absorption. As a result, reflection removal becomes an ill-posed inverse problem, where the solution is not unique or stable. To constrain the solution space and obtain a globally optimal solution, it is essential to incorporate prior knowledge or introduce image sequences with different characteristics.

According to Fresnel theory[37,38], diffuse reflection is unpolarized light, while specular reflection is partially polarized light. Therefore, as the polarization direction changes, the diffuse component remains constant, whereas the specular component varies. According to the polarization-reflection model derived from Malus' law, specular reflection tends to carry the characteristics of reflected light from the ambient light source and scene, while diffuse reflection reveals the surface details and morphological features of the object. The diffuse reflection light from the face becomes partially polarized refracted light after passing through the eyeglass. Thus, both the transmitted and reflected light entering the camera are partially polarized. After polarization filtering, images captured at different linear polarization directions can be expressed as follows:

$$\boldsymbol{I}_{\theta}(x)=\boldsymbol{A}_{\theta}(x)\,\boldsymbol{I}_{\mathrm{B}}(x)+(1-\boldsymbol{A}_{\theta}(x))\,\boldsymbol{I}_{\mathrm{R}}(x)\ , \tag{2}$$

where $\boldsymbol{A}_{\theta}$ denotes a matrix with the same dimensions as $\boldsymbol{I}_{\theta}$, which is associated with the polarization filter direction.

When light is incident at the Brewster angle, the P-polarized component of reflected light becomes zero, and the reflected light is S-polarized. As a result, the reflected light is linearly polarized and can be removed physically using linear polarization filter. However, the angle of incidence does not always match the Brewster angle. Therefore, this work aims to estimate the transmission layer through polarization-based computation to achieve reflection removal. A Sony division-of-focal-plane color polarization sensor is used to capture the images corresponding to four linear polarization directions in one shot: 0°, 45°, 90°, and 135°. The Stokes parameters can be calculated from these four linear polarization directions.

Using the Stokes parameters, intensity images at any linear polarization direction can be synthesized,

$$\boldsymbol{I}'_{\theta}=\frac{\boldsymbol{S}_0}{2}+\frac{\boldsymbol{S}_1}{2}\cos 2\theta+\frac{\boldsymbol{S}_2}{2}\sin 2\theta\ . \tag{3}$$

As shown in Fig. 2, the intensity images under different polarization directions exhibit varying proportions of the transmission and reflection layers, which is consistent with Eq. (2). This provides additional constraints for solving the ill-posed problem of transmission image. Compared to transmitted light, reflected light typically exhibits the higher DoLP. Therefore, reflection regions can be preliminarily identified using DoLP. The transmission and reflection layers can be separated by leveraging the differences in their polarization characteristics[39].

2.2 Polarization-guided diffusion prior for reflection removal

The framework of the proposed polarization-guided

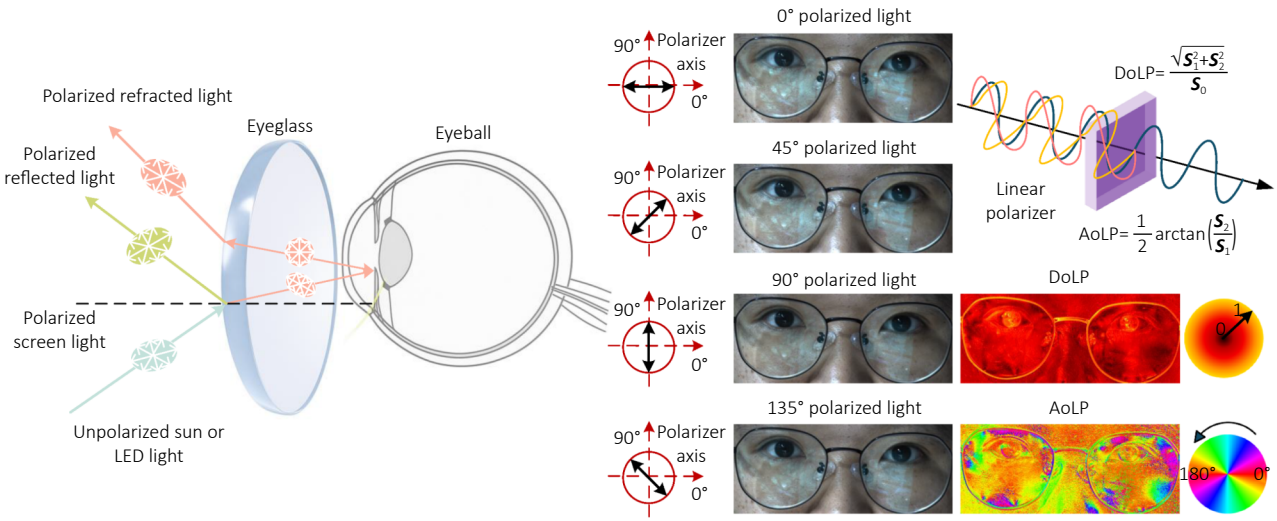


Fig. 2 | Principle of polarization for suppressing eyeglass reflection. Left: polarization state differences between transmitted and reflected light. Right: polarization characteristics of transmitted and reflected light as observed in images captured at different polarization directions.

diffusion prior for eyeglass reflection removal is illustrated in Fig. 3. This framework requires neither large-scale training datasets nor paired reflection/reflection-free training images. Given that diffusion model has outperformed GANs[40] in image generation tasks —with fewer artifacts, higher fidelity, and more stable training —this work leverages diffusion model to generate reflection-free images. During the reverse sampling process of the diffusion model, both the reflection and transmission layers are iteratively updated. By combining the diffusion prior with polarization constraints, the PDPrior enables joint estimation of transmission and reflection images without any training, using only the polarization observations from test samples. Through intensity, gradient, and entropy constraints, the optimal linear polarization direction is adaptively selected and used as input for the transmission diffusion model to further remove reflection. The DoLP is used to identify potential reflection regions, guiding the reflection generation model to focus on these areas. Moreover, using the DoLP to compute the transmission coefficient, the generation of transmission image is guided by the physical forward model of reflection formation, ensuring that the generation model is physically interpretable.

The transmission reverse generation process refers to the gradual removal of reflection, while the reflection reverse generation process refers to the gradual removal of transmission. Taking the transmission reverse generation process as an example, the process of sampling reflection-free data $\boldsymbol{x}_{t-1}$ from $\boldsymbol{x}_t$ is defined as follows:

$$p_\omega\left(\boldsymbol{x}_{T-1:\,0}|\boldsymbol{x}_T\right)=\prod_{t=1}^{T}p_\omega\left(\boldsymbol{x}_{t-1}|\boldsymbol{x}_t\right)\ , \tag{4}$$

$$p_\omega\left(\boldsymbol{x}_{t-1}|\boldsymbol{x}_t\right)=\mathcal{N}\left(\boldsymbol{x}_{t-1};\mu\left(\boldsymbol{x}_t,t\right),\Sigma\boldsymbol{E}\right)\ , \tag{5}$$

where $p_\omega\left(\boldsymbol{x}_{t-1}|\boldsymbol{x}_t\right)$ denotes the target distribution of the generative model, the variance Σ can either be a learnable parameter[40] or remain fixed as a hyperparameter[41]. The Σ is derived from the posterior distribution and is set as a time-dependent constant. T denotes the total number of steps in the diffusion process, and t represents the current step in the generation process. $\boldsymbol{E}$ denotes the ones matrix. ε_ω represents the neural network. The U-Net[42] is used as the function approximator, which takes $\boldsymbol{x}_t$ as input and outputs the predicted value of noise. $\tilde{\boldsymbol{x}}_0$ can be computed from $\boldsymbol{x}_t$ and $\varepsilon_\omega\left(\boldsymbol{x}_t,t\right)$,

$$\tilde{\boldsymbol{x}}_0=\frac{\boldsymbol{x}_t}{\sqrt{\overline{\alpha}_t}}-\frac{\sqrt{1-\overline{\alpha}_t}\varepsilon_\omega\left(\boldsymbol{x}_t,t\right)}{\sqrt{\overline{\alpha}_t}}\ . \tag{6}$$

Compute the transmission mean $\boldsymbol{\mu}_t$ using $\boldsymbol{x}_t$ and $\tilde{\boldsymbol{x}}_0$ by

$$\boldsymbol{\mu}_t=\frac{\sqrt{\overline{\alpha}_{t-1}}\beta_t}{1-\overline{\alpha}_t}\tilde{\boldsymbol{x}}_0+\frac{\sqrt{\alpha_t}\left(1-\overline{\alpha}_{t-1}\right)\beta_t}{1-\overline{\alpha}_t}\boldsymbol{x}_t\ . \tag{7}$$

Then, based on $\boldsymbol{\mu}_t$, $\boldsymbol{x}_{t-1}$ can be inferred by

$$\boldsymbol{x}_{t-1}=\boldsymbol{\mu}_t+\sqrt{\tilde{\beta}_t}\boldsymbol{\sigma}\ . \tag{8}$$

In the reverse generation process, the reflection and transmission images are updated at each iteration. The parameters of the U-Net are randomly initialized. The DoLP can also be expressed as:

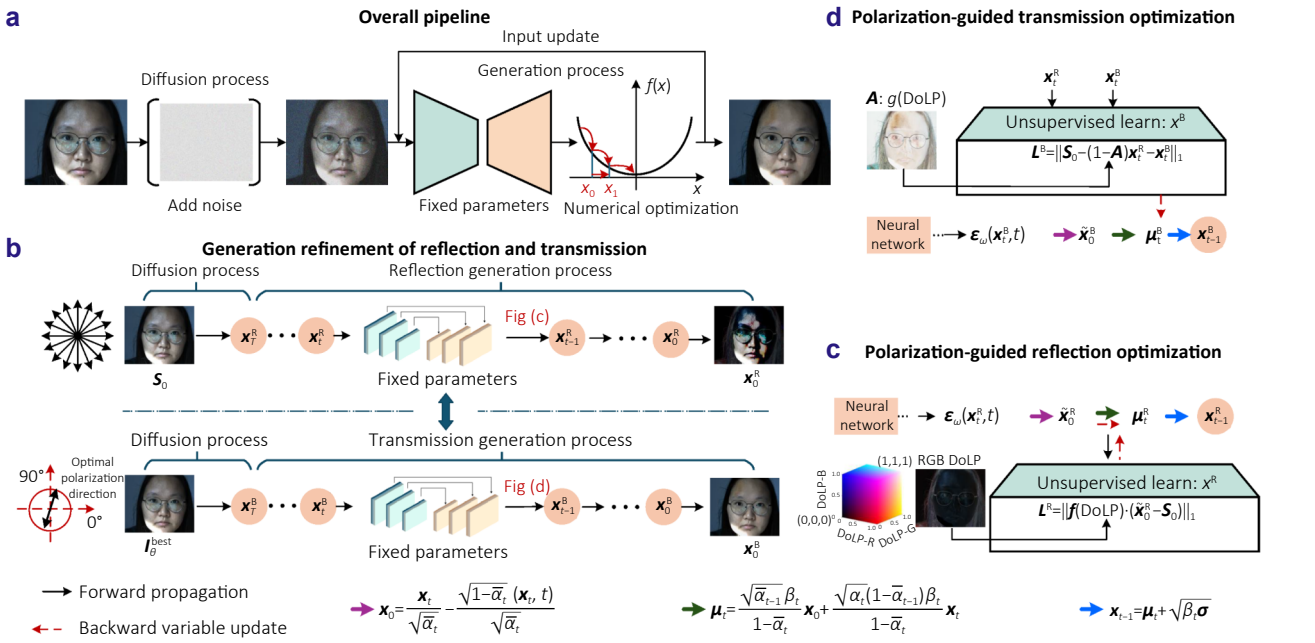


Fig. 3 | Flowchart of the PDPrior. (a) Overall pipeline of the PDPrior. (b) Generation refinement of reflection and transmission. (c) Flowchart of polarization-guided reflection optimization. (d) Flowchart of polarization-guided transmission optimization.

$$DoLP=\frac{\boldsymbol{I}_{\parallel}-\boldsymbol{I}_{\perp}}{\boldsymbol{I}_{\parallel}+\boldsymbol{I}_{\perp}}\ , \tag{9}$$

where $\boldsymbol{I}_{\parallel}$ and $\boldsymbol{I}_{\perp}$ are two intensity images captured under orthogonal polarization states.

The transmission coefficient $\boldsymbol{A}$ can be expressed as:

$$\boldsymbol{A}\left(x\right)=1-c_1\left(x\right)\left(\boldsymbol{I}(x)_{\parallel}-\boldsymbol{I}(x)_{\perp}\right)\ . \tag{10}$$

Therefore, the relationship between the transmission coefficient and the DoLP can be established as follows:

$$\begin{aligned}&\boldsymbol{A}_0=1-c_2DoLP\\&\boldsymbol{M}=\begin{cases}0.5 & 1-\boldsymbol{I}_{\theta}^{\text{best}}\in(0\text{–}0.5,0\text{–}0.3,0\text{–}0.1)\\1.0 & \text{others}\end{cases}\\&\boldsymbol{A}=g\left(DoLP\right)=\boldsymbol{M}\odot\tanh\left(\frac{2\cdot\mathrm{e}^{5\cdot\boldsymbol{A}_0}}{\mathrm{e}^5}\right)\ .\end{aligned} \tag{11}$$

The value of c_2 is set to 1. (0–0.5, 0–0.3, 0–0.1) represents the threshold values for three color channels (R, G, B). $\boldsymbol{M}$ is computed using the color prior to reduce the transmission coefficients in strong reflection area.

We collected facial images of individuals wearing glasses under diverse lighting conditions, including indoor illumination, display screen light, and sunlight. According to Eq. (3), the intensity images at polarization angles ranging from 0° to 180° in 5° increments are synthesized. The image with the weakest reflection was manually selected as the optimal polarization direction based on visual assessment. Experimental observations show that, compared to other polarization directions, the optimal direction image exhibits lower brightness, and due to the suppression of reflected light, the edge textures in reflective scenes become less distinct. Leveraging these characteristics, we designed the objective function in Eq. (12), which jointly considers image intensity, gradient magnitude, and information entropy to dynamically select the optimal polarization direction.

$$\min_{\theta}\left[L\left(\boldsymbol{I}_{\theta}'\right)\times G\left(\boldsymbol{I}_{\theta}'\right)\times\boldsymbol{IE}\left(\boldsymbol{I}_{\theta}'\right)\right]\ , \tag{12}$$

where L denotes the average intensity of the image, G represents the average gradient magnitude, and $\boldsymbol{IE}$ refers to the information entropy. As shown in Fig. 4(a), we selected three face images captured under different lighting conditions and plotted their curves with respect to the polarization direction. As illustrated in Fig. 4(b), human judgment is used to select the optimal polarization angle, from 0° to 180°, corresponding to the image with the minimal reflection. By comparing Fig. 4(a) and 4(b), it can be observed that the polarization angle corresponding to the minimum value of the metric defined in Eq. (12) aligns with the optimal polarization angle determined by human observers, demonstrating the effectiveness of Eq. (12). The intensity image $\boldsymbol{I}_{\theta}^{\text{best}}$ under the selected optimal polarization direction is used as the input to the transmission diffusion model for further reflection removal.

As shown in Fig. 3(b), the reflection diffusion process takes the unpolarized intensity image $\boldsymbol{S}_0$ as input and adds noise through a Markov chain. The transmission diffusion process uses the intensity image $\boldsymbol{I}_{\theta}^{\text{best}}$ as input and similarly adds noise via a Markov chain, with the number of steps T set to 8. The criteria for determining T is provided in Section 3 of the Supplementary information.

We observed that, without any constraints, an untrained diffusion model tends to gradually darken the facial region starting from the contours during the iterative generation process. Based on this generative prior, we leverage the DoLP to construct an attention map that accelerates the darkening of non-reflective areas and enhances the brightness of reflective regions, thereby guiding the reflection generation model to focus more on the eyeglass reflection. Utilizing this prior, we design the following loss function to update the reflection image via gradient descent during the reverse generation process.

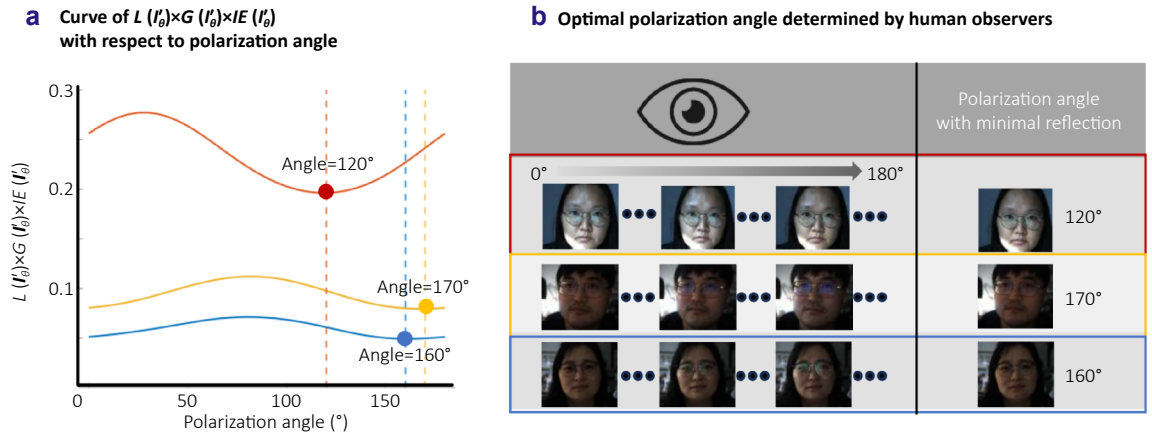


Fig. 4 | Comparison with the optimal polarization angle selected by $\min_{\theta}\left[L\left(\boldsymbol{I}_{\theta}'\right)\times G\left(\boldsymbol{I}_{\theta}'\right)\times\boldsymbol{IE}\left(\boldsymbol{I}_{\theta}'\right)\right]$ and human observers. (a) Curve of $L\left(\boldsymbol{I}_{\theta}'\right)\times G\left(\boldsymbol{I}_{\theta}'\right)\times\boldsymbol{IE}\left(\boldsymbol{I}_{\theta}'\right)$ with respect to polarization angle. The solid line represents the value of $L\left(\boldsymbol{I}_{\theta}'\right)\times G\left(\boldsymbol{I}_{\theta}'\right)\times\boldsymbol{IE}\left(\boldsymbol{I}_{\theta}'\right)$ under any polarization-angle intensity image calculated from the four linearly polarized images according to Eq. (3). The circle marks the minimum of the curve. (b)The optimal polarization direction determined by human observers.

$$\boldsymbol{L}^{\mathrm{R}} = \left|\left| f(DoLP) \cdot \left(\tilde{\boldsymbol{x}}_0^{\mathrm{R}} - \boldsymbol{S}_0\right)\right|\right|_1, \tag{13}$$

$$f(DoLP) = \mathrm{e}^{k\cdot(1-DoLP)}, \tag{14}$$

where k is set to 5. $f(\cdot)$ assigns higher weights to regions with low degrees of polarization (non-reflective areas) and lower weights to regions with high degrees of polarization (reflective areas).

Based on the forward model of Eq. (1), the following loss function is established to achieve the separation of the transmission and reflection layers.

$$\boldsymbol{L}^{\mathrm{B}} = \left\|\boldsymbol{S}_0 - (1-\boldsymbol{A})\,\boldsymbol{x}_t^{\mathrm{R}} - \boldsymbol{x}_t^{\mathrm{B}}\right\|_1. \tag{15}$$

Algorithm 1: The PDPrior algorithm for eyeglass reflection removal

Input: the linear polarization intensity images $\boldsymbol{I}_0$, $\boldsymbol{I}_{45}$, $\boldsymbol{I}_{90}$, $\boldsymbol{I}_{135}$; T=8

1: Calculate DoLP.

2: Calculate $\boldsymbol{I}_\theta^{\mathrm{best}}$ by Eq. (3) and Eq (12).

3: Initialization of reflection diffusion process: $\boldsymbol{S}_0$; Initialization of transmission diffusion process: $\boldsymbol{I}_\theta^{\mathrm{best}}$.

4: Add noise in $\boldsymbol{S}_0$ and $\boldsymbol{I}_\theta^{\mathrm{best}}$ by the forward diffusion process to obtain $\boldsymbol{x}_T^{\mathrm{R}}$ and $\boldsymbol{x}_T^{\mathrm{B}}$.

5: Initialization of reflection generation process: $\boldsymbol{x}_T^{\mathrm{R}}$; Initialization of transmission generation process: $\boldsymbol{x}_T^{\mathrm{B}}$.

6: for t=T–1 to 1 do

7: $\boldsymbol{\sigma} \sim \mathcal{N}(0, \boldsymbol{E})$ if $t > 1$, else $\boldsymbol{\sigma} = 0$

8: Estimate $\tilde{\boldsymbol{x}}_0^{\mathrm{R}}$ by Eq. (6)

9: Update $\boldsymbol{\mu}_t^{\mathrm{R}}$ by Eq. (13)

10: Calculate $\boldsymbol{x}_{t-1}^{\mathrm{R}}$ by Eq. (8)

11: Estimate $\tilde{\boldsymbol{x}}_0^{\mathrm{B}}$ by Eq. (6)

12: Update $\boldsymbol{\mu}_t^{\mathrm{B}}$ by Eq. (15)

13: Calculate $\boldsymbol{x}_{t-1}^{\mathrm{B}}$ by Eq. (8)

14: end for

return: $\boldsymbol{x}_0^{\mathrm{R}}$, $\boldsymbol{x}_0^{\mathrm{B}}$.

3 Results

3.1 Polarization image acquisition

As shown in Fig. 5, a Sony IMX250MYR CMOS color sensor is employed to perform snapshot imaging under four linear polarization directions (0°, 45°, 90°, and 135°) and three color channels (R, G, B). A computar lens with 16 mm focal length is mounted in front of the polarization camera. The polarization sensor is a 2048×2448 pixel array composed of repeating 4×4 super pixels. This array is decomposed by grouping pixels with the same polarization orientation into an RGGB Bayer pattern, followed by color demosaicing to obtain a 1024×1224 color image for each polarization direction. Consequently, each exposure captures color images under the four polarization angles: 0°, 45°, 90°, and 135°. The face images with eyeglasses were collected in both indoor and outdoor environments. Indoor lighting consists of the LED light source combined with the display screen primarily, where the screen is the polarized light source. The imaging setup is positioned in front of the screen. In outdoor environments, sunlight, which is unpolarized, serves as the primary illumination source, and handheld selfies are captured. These setups are designed to simulate typical lighting conditions encountered during indoor and outdoor video conferencing or facial recognition scenarios.

3.2 Experimental results

The proposed method, PDPrior, was compared with both single-image and polarization-based reflection removal algorithms that have publicly available source codes. Although DL2G[18] targets eyeglass reflection removal, its source code has not been released and thus cannot be included for comparison. Therefore, the single-image reflection removal methods used for comparison include Wen's method[43], DoubleDIP[14], and RDNet[44]. The Wen's method is referred to as SIRRBL. DoubleDIP is an untrained reflection removal method based on deep image priors, while SIRRBL and RDNet are supervised learning approaches. SIRRBL utilizes a synthesis network, SynNet, to generate simulated training images for supervised learning. RDNet's training dataset comprises both real and synthetic images. The polarization-based methods include PolarHR[28] and PolarFree[33]. PolarHR is an ADMM-based optimization algorithm derived from physical modeling, whereas PolarFree is a diffusion-based supervised method trained on real paired polarization data. Due to the limited availability of reflection synthesis pipelines and the large gap between synthetic and real polarization images, all methods are directly evaluated on real-world images. All experiments are conducted on a GV100 GPU, except for PolarHR, which is run on the MATLAB platform. Except for DoubleDIP, for the single-image methods, the input is the unpolarized intensity image $\boldsymbol{S}_0$. Since DoubleDIP requires two images with different mixing ratios of the transmission and reflection layers, the two images are captured at 0° and 90° linear polarization, respectively. For the polarization-based methods, the input consists of four color images captured at polarization angles of 0°, 45°, 90°, and 135°. For the PDPrior, the input image is divided into m×n blocks of size 256×256 to enable reflection removal on images of arbitrary size. An overlap ratio of 0.125 between adjacent blocks is applied to improve runtime efficiency while maintaining performance. The rationale for the choice of block size and overlap ratio is provided in Section 4 and

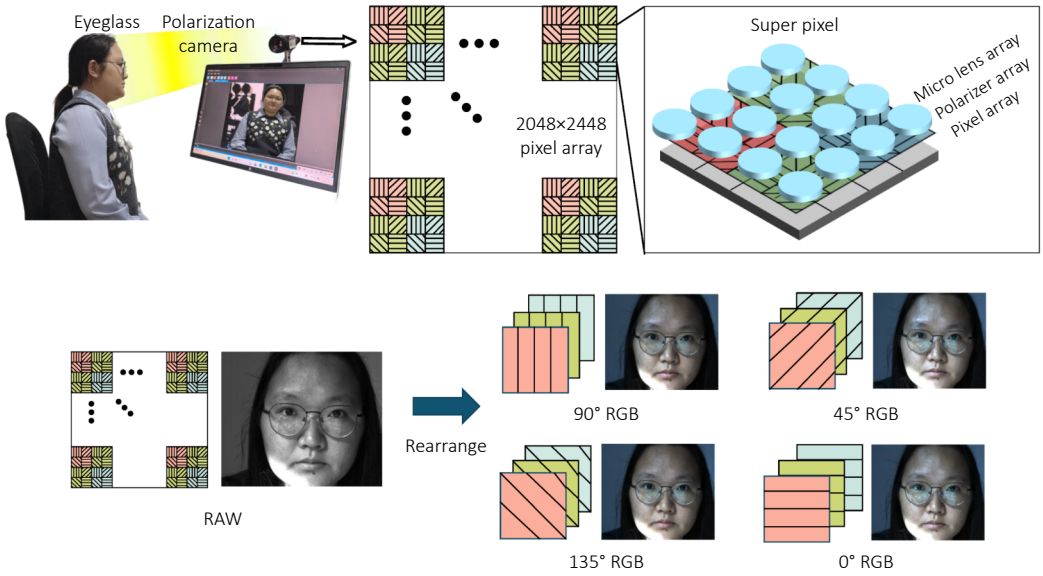


Fig. 5 | Experimental setup for image acquisition: division of focal plane polarization camera, using a 4×4 super pixel structure that contains three color channels (R, G, B) and four linear polarization directions (0°, 45°, 90°, and 135°).

Section 5 of the Supplementary information.

Figure 6 shows the eyeglass reflection removal results on facial images captured using the device illustrated in Fig. 5 under various lighting conditions. The first four rows correspond to indoor lighting (LED and display screen), while the last two rows represent outdoor sunlight condition. As observed from Fig. 6, compared with the first column of unpolarized intensity images, the second column, using the optimal polarization direction adaptively selected via proposed Eq. (12), can eliminate part of the reflection. However, under strong outdoor illumination, the reflection suppression achieved through physical polarization filter remains limited. Columns three to five show the results of single-image reflection removal methods. SIRRBL fails to remove reflection effectively. DoubleDIP tends to introduce severe artifacts, especially under strong lighting, as seen in the fifth and sixth rows. RDNet removes reflection but causes noticeable color distortions. Columns six and seven display the results of polarization-based reflection removal methods. PolarHR performs relatively well under outdoor conditions but introduces artifacts under indoor lighting. PolarFree fails to effectively eliminate eyeglass reflections and generates artifacts in the eye region, as shown in the fifth and sixth rows, while also blurring background details, as seen in the third row. The eighth column presents the results of the proposed untrained method of PDPrior. The PDPrior successfully removes eyeglass reflection while preserving the transmission scene content, achieving artifact-free, and high-fidelity reflection removal. By comparing the last two rows of Fig. 6 and the Fig. 1 with the results before and after reflection removal, it can be observed that images containing specular reflections exhibit a bluish-green color tone. Since the illumination source in the experiments is white light, the influence of the light source on the color bias can be excluded. The bluish-green appearance mainly originates from specular reflections on the facial surface, which possess polarization characteristics. Moreover, polarization is wavelength-dependent, leading to bluish-green color shifts. According to the study "Characterising the variations in ethnic skin colours"[45], the skin color distribution of Chinese populations is relatively compact, with Yellowness values lying in a medium-to-high range. After removing specular reflections, the facial images reconstructed by PDPrior exhibit a more yellowish skin tone, which aligns well with established skin color statistics and human perceptual expectations. From the perspectives of color consistency and facial skin color priors, this provides further evidence that the PDPrior reconstruction yields results that are closer to the true scene.

Currently, there are no publicly available polarized datasets targeting eyeglass reflection, making it infeasible to conduct quantitative evaluation on benchmark data. To address this, we collected and released 27 groups of polarized face images with eyeglass reflections as the test dataset①, named PolarGlass. The details and representative samples of PolarGlass are illustrated and presented in Section 7 of the Supplementary Material. Moreover, the face quality assessment methods[46,47] are adopted to quantitatively evaluate the 27 groups of reconstructed face images. Face quality assessment aims to estimate the suitability of a face image for

① https://cloud.tsinghua.edu.cn/f/a49e0f59a8a54c4eb14d/?dl=1

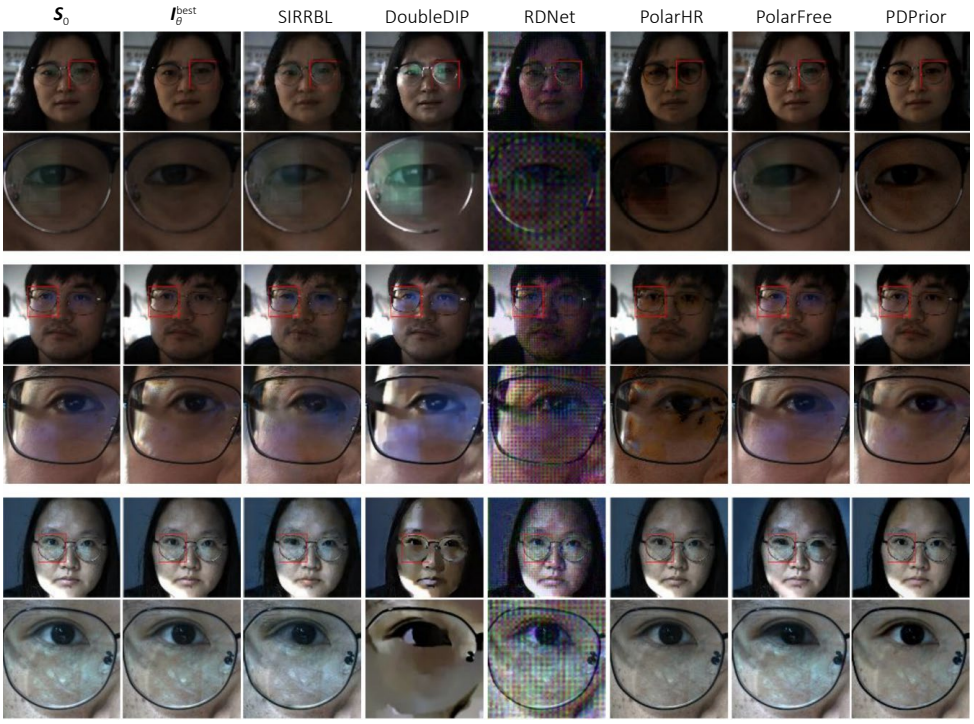


Fig. 6 | Reflection removal results using the setup shown in Fig. 5. The first column shows unpolarized intensity images. The second column presents the images with the optimal polarization direction adaptively selected using the proposed Eq. (12). Columns three to five show results of single-image reflection removal methods. Columns six and seven display results of polarization-based reflection removal methods. The eighth column shows the results of PDPrior.

recognition. As shown in Table 1, the PDPrior achieves overall higher face quality assessment scores. Compared with the untrained method DoubleDIP, PDPrior reduces the runtime by approximately 536 times. Although RDNet performs slightly better than PDPrior in CLIB-FIQA, the qualitative results in Fig. 6 indicate that CLIB-FIQA fails to account for color distortion artifacts and only reflects the sharpness and texture quality of the reconstructed face. Figure 7 presents the violin plot of the 27 reconstructed faces, where the central star denotes the mean and the bar length indicates the variance. The PDPrior not only yields a higher mean but also exhibits a smaller variance, demonstrating the robustness of eyeglass reflection removal. The polarization imaging effectively suppress glare and enhance target contrast compared with RGB imaging[48]. But certain polarization directions may still suffer from overexposure under strong illumination conditions. In overexposed regions, the captured polarized intensity images are clipped representations of the true scene luminance, meaning that the recorded pixel values cannot accurately reflect the actual brightness. As a result, the polarization characteristics computed from the 0°/45°/90°/135° linear polarization intensity images (e.g., degree and angle of linear polarization) may not correspond to the true polarization characteristics of the scene, rendering polarization unable to provide reliable priors for reflective regions. Consequently, polarization-based reflection removal methods may fail in overexposed areas.

3.3 Diffusion prior study

The reflection regions typically exhibit high brightness and strong polarization, whereas the background regions have lower brightness and weaker polarization. During the reflection image generation process, the diffusion prior can effectively exploit this property. Furthermore, we design a weighting function $f(DoLP)$, as shown in Eq. (14) to enhance this prior, assigning lower weights to regions with

Table 1 | Quantitative comparison on the real eyeglass reflection data.

	SIRRBL	DoubleDIP	RDNet	PolarHR	PolarFree	PDPrior(Ours)
CR-FIQA↑	1.32	1.13	1.19	1.30	1.34	**1.37**
CLIB-FIQA↑	0.53	0.48	**0.57**	0.53	0.54	0.55
Time / s↓	**1.68**	4834	5.03	39.59	2.25	9.00

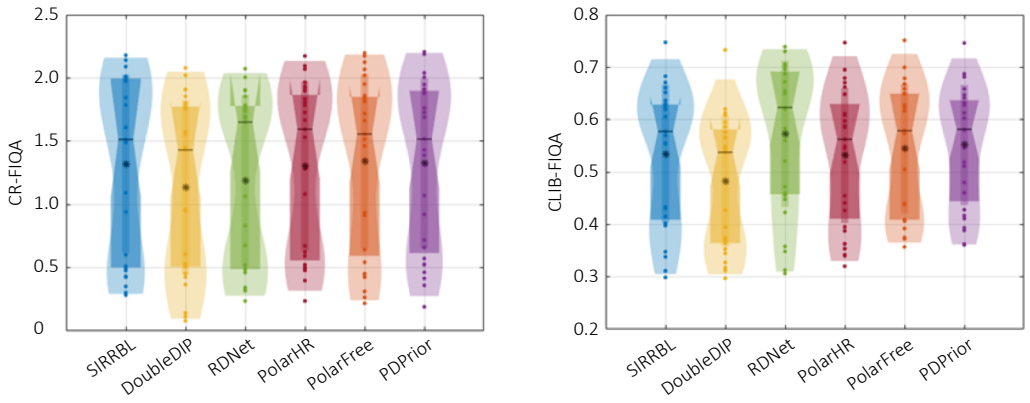


Fig. 7 | CR-FIQA and CLIB-FIQA are neural network-based methods for the estimation of face image quality, aimed at assessing face recognition performance.

high polarization degrees and higher weights to regions with low polarization degrees. Since the reflection generation branch takes $\boldsymbol{S}_0$ both as the input and as the self-supervised target, the model prioritizes the adjustment of high-weight background areas during the minimization of the loss, driving their intensity values toward zero. Meanwhile, the low-weight, reflection regions are preserved, thereby achieving effective modeling of the reflection components. During optimization, the reflection and transmission images are updated alternately. The transmission generation branch takes the image corresponding to the optimal polarization direction with minimal reflection as input, by leveraging the generated reflection image together with the forward model of reflection formation, gradually approaches a reflection-free transmission image $\boldsymbol{S}_0 - (1 - \boldsymbol{A})\,\boldsymbol{x}_t^{\mathrm{R}}$.

The first column in Fig. 8(a) illustrates the generation process of reflection images without any constraints. It can be observed that the process gradually darkens the facial region. The PDPrior leverages this diffusion prior. The second column in Fig. 8(a) presents the reflection image generation processes of PDPrior. Compared to the first column, the reflection generation of the second column focuses more on the reflection regions, further darkening the reflection-free areas while enhancing the reflection. Figure 8(b) illustrates the convergence behavior of the data loss of forward model corresponding to Eq. (15) for the 27 reconstructed face during the reverse generation process. From t=7 to t=3, the loss drops sharply and then gradually levels off. By examining the generation transmission and reflection images at the indicated t values alongside the curve of Fig. 8(b), it can be observed that the reflective components in the transmission images are progressively removed. The generation results are generally consistent with the data loss trend.

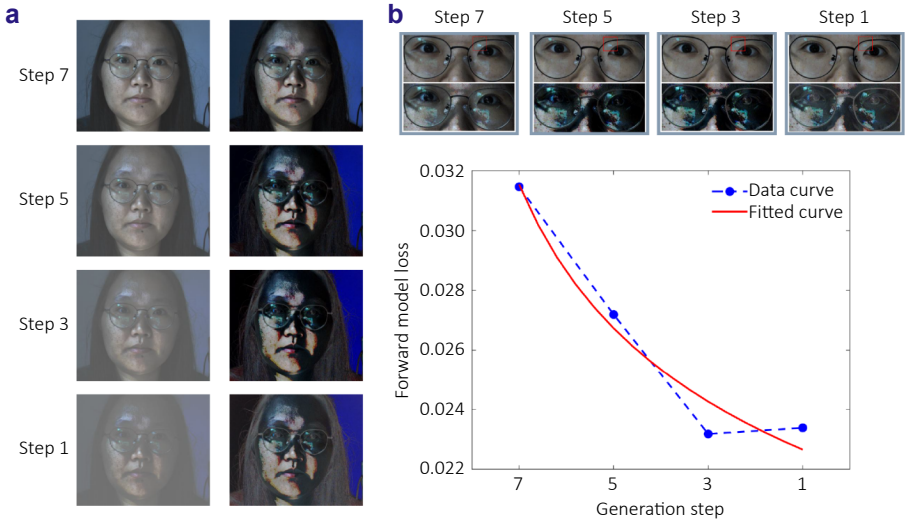


Fig. 8 | Reflection generation and convergence analysis. (a) Reflection generation process. The first column shows the unconstrained reflection image generation process, and the second column shows the PDPrior reflection image generation process. (b) Convergence process of data loss, along with generation transmission image $\boldsymbol{x}_t^{\mathrm{B}}$ and reflection image $\boldsymbol{x}_t^{\mathrm{R}}$. The horizontal axis represents the reverse generation process from T-1 to 0, while the vertical axis shows the data loss of forward model in Eq. (15). The grayscale values of the input image are normalized to [0, 1].

We evaluated PDPrior using U-Net architectures with varying numbers of layers and feature channels, examining their runtime, memory usage, and reflection removal performance. It is shown that a compact U-Net architecture is sufficient to achieve the desired task performance, a phenomenon also observed in DIP[13]. Detailed information on the U-Net architectures and the PDPrior's performance can be found in Section 6 of the Supplementary Material. The memory consumption of PDPrior is 2.04 GB, and the runtime is 9.00 seconds for 1024×1224 polarization data on a GV100 GPU, including both the diffusion and generation processes. To enhance the practical deployment of PDPrior on resource-constrained devices, future work will focus on reducing memory usage and runtime. The forward diffusion and reverse generation processes could be performed in the latent space rather than the pixel space to significantly decrease computational cost. The model pruning and knowledge distillation techniques could be applied to compress the model size without notable performance degradation. The CUDA-based parallel acceleration and mixed-precision computation could be applied to further improve inference efficiency and resource utilization.

4 Conclusions

To tackle the challenge of eyeglass reflection obscuring facial features, we propose an untrained polarization reflection removal method, PDPrior. The PDPrior requires no training data, and no ground-truth reflection-free images. The PDPrior leverages the generative prior of a diffusion model and introduces polarization information as guidance to control the generation process. The reflection diffusion model utilizes the DoLP to preliminarily identify reflection regions and the diffusion prior of progressively darkening facial content during the generation process, enabling the model to focus on reflective regions. Using the DoLP to compute the transmission coefficient, the generation of transmission image is guided by the physical forward model of reflection formation. During each sampling step, the reflection and transmission variables are alternately and iteratively updated via gradient descent based solely on the test sample, making PDPrior more adaptable to complex lighting conditions and diverse scenes. We collected real-world eyeglasses reflection images using a division-of-focal-plane polarization camera under various indoor and outdoor lighting environments. Experimental results demonstrate that PDPrior effectively removes eyeglass reflection, producing high-fidelity face reconstructions with no visible artifacts and achieving more robust face image quality assessment scores for recognition performance. The PDPrior provides a general framework for reflection removal, which can be extended to diverse real-world scenarios such as window photography, showcase displays, and driver monitoring, paving the way for broader applications in consumer photography and intelligent vision systems.

References

1. Wan RJ, Shi BX, Duan LY et al. Region-aware reflection removal with unified content and gradient priors. *IEEE Trans Image Process* **27**, 2927–2941 (2018).
2. Gao YH, Cao LC. Iterative projection meets sparsity regularization: towards practical single-shot quantitative phase imaging with in-line holography. *Light Adv Manuf* **4**, 37–53 (2023).
3. Yang Y, Ma WY, Zheng Y et al. Fast single image reflection suppression via convex optimization. In *Proceedings of the IEEE/CVF Conference on Computer Vision and Pattern Recognition* 8133–8141 (IEEE, 2019). https://doi.org/10.1109/CVPR.2019.00833.
4. Gao YH, Cao LC. Generalized optimization framework for pixel super-resolution imaging in digital holography. *Opt Express* **29**, 28805–28823 (2021).
5. Jin Z, Qiu YW, Zhang KH et al. MB-TaylorFormer V2: improved multi-branch linear transformer expanded by Taylor formula for image restoration. *IEEE Trans Pattern Anal Mach Intell* **47**, 5990–6005 (2025).
6. Fei B, Lyu ZY, Pan L et al. Generative diffusion prior for unified image restoration and enhancement. In *Proceedings of the IEEE/CVF Conference on Computer Vision and Pattern Recognition* 9935–9946 (IEEE, 2023). https://doi.org/10.1109/CVPR52729.2023.00958.
7. Zhang KH, Wang T, Luo WH et al. MC-blur: a comprehensive benchmark for image deblurring. *IEEE Trans Circuits Syst Video Technol* **34**, 3755–3767 (2024).
8. Zhang KH, Luo WH, Zhong YR et al. Adversarial spatio-temporal learning for video deblurring. *IEEE Trans Image Process* **28**, 291–301 (2019).
9. Sandhan T, Choi JY. Anti-glare: tightly constrained optimization for eyeglass reflection removal. In *Proceedings of the IEEE Conference on Computer Vision and Pattern Recognition* 1675–1684 (IEEE, 2017). https://doi.org/10.1109/CVPR.2017.182.
10. Zhang XE, Ng R, Chen QF. Single image reflection separation with perceptual losses. In *Proceedings of the IEEE/CVF Conference on Computer Vision and Pattern Recognition* 4786–4794 (IEEE, 2018). https://doi.org/10.1109/CVPR.2018.00503.
11. Zou WT, Lu X, Yi ZL et al. Eyeglass reflection removal with joint learning of reflection elimination and content inpainting. *IEEE Trans Circuits Syst Video Technol* **34**, 10266–10280 (2024).
12. Li C, Yang YX, He K et al. Single image reflection removal through cascaded refinement. In *Proceedings of the IEEE/CVF Conference on Computer Vision and Pattern Recognition* 3562–3571 (IEEE, 2020). https://doi.org/10.1109/CVPR42600.2020.00362.
13. Huang JJ, Liu TR, Chen ZH et al. A lightweight deep exclusion unfolding network for single image reflection removal. *IEEE Trans Pattern Anal Mach Intell* **47**, 4957–4973 (2025).
14. Gandelsman Y, Shocher A, Irani M. "Double-DIP": unsupervised image decomposition via coupled deep-image-priors. In *Proceedings of the IEEE/CVF Conference on Computer Vision and Pattern Recognition* 11018–11027 (IEEE, 2019). https://doi.org/10.1109/CVPR.2019.01128.
15. RahmaniKhezri H, Kim S, Hefeeda M. Unsupervised single-image reflection removal. *IEEE Trans Multimedia* **25**, 4958–4971 (2023).
16. Rosh G, Prasad BHP, Boregowda LR et al. Deep unsupervised reflection removal using diffusion models. In *2023 IEEE International Conference on Image Processing* 2045–2049 (IEEE, 2023). https://doi.org/10.1109/ICIP49359.2023.10222641.

17. Wang T, Lu WL, Zhang KH et al. PromptRR: diffusion models as prompt generators for single image reflection removal. *arXiv preprint* arXiv: 2402.02374 (2024). https://doi.org/10.48550/arXiv.2402.02374
18. Yi ZL, Lu X, Ding H et al. DL2G: degradation-guided local-to-global restoration for eyeglass reflection removal. In *Proceedings of the IEEE/CVF Conference on Computer Vision and Pattern Recognition* 16061–16070 (IEEE, 2025). https://doi.org/10.1109/CVPR52734.2025.01497.
19. Lei CY, Chen QF. Robust reflection removal with reflection-free flash-only cues. In *Proceedings of the IEEE/CVF Conference on Computer Vision and Pattern Recognition* 14806–14815 (IEEE, 2021). https://doi.org/10.1109/CVPR46437.2021.01457.
20. Wang TF, Xie MY, Cai HM et al. Flash-split: 2D reflection removal with flash cues and latent diffusion separation. In *Proceedings of the IEEE/CVF Conference on Computer Vision and Pattern Recognition* 5688–5698 (IEEE, 2025). https://doi.org/10.1109/CVPR52734.2025.00534.
21. Shi WQ, Quan HD, Kong LB. Adaptive specular reflection removal in light field microscopy using multi-polarization hybrid illumination and deep learning. *Opt Lasers Eng* **186**, 108839 (2025).
22. Rubin NA, D'Aversa G, Chevalier P et al. Matrix Fourier optics enables a compact full-Stokes polarization camera. *Science* **365**, eaax1839 (2019).
23. Fan QB, Xu WZ, Hu XM et al. Disordered metasurface enabled single-shot full-Stokes polarization imaging leveraging weak dichroism. *Nat Commun* **14**, 7180 (2023).
24. Zhang YX, Pu MB, Jin JJ et al. Crosstalk-free achromatic full Stokes imaging polarimetry metasurface enabled by polarization-dependent phase optimization. *Opto-Electron Adv* **5**, 220058 (2022).
25. Zhang HF, Zhang XQ, Xu Q et al. High-efficiency dielectric metasurfaces for polarization-dependent terahertz wavefront manipulation. *Adv Opt Mater* **6**, 1700773 (2018).
26. Liu MZ, Huo PC, Zhu WQ et al. Broadband generation of perfect Poincaré beams via dielectric spin-multiplexed metasurface. *Nat Commun* **12**, 2230 (2021).
27. Gigan S. Data-driven polarimetric approaches fuel computational imaging expansion. *Opto-Electron Adv* **7**, 240158 (2024).
28. Wen SJ, Zheng YQ, Lu F. Polarization guided specular reflection separation. *IEEE Trans Image Process* **30**, 7280–7291 (2021).
29. Wang X, Zhang Y, Chen YC. Polarized reflection removal with dual-stream attention guidance. *Pattern Recognit* **157**, 110945 (2025).
30. Wieschollek P, Gallo O, Gu JW et al. Separating reflection and transmission images in the wild. In *Proceedings of the 15th European Conference on Computer Vision* 90–105 (Springer, 2018). https://doi.org/10.1007/978-3-030-01261-8_6.
31. Li R, Qiu SM, Zang GM et al. Reflection separation via multi-bounce polarization state tracing. In *Proceedings of the 16th European Conference on Computer Vision* 781–796 (Springer, 2020). https://doi.org/10.1007/978-3-030-58601-0_46.
32. Lei CY, Huang XH, Zhang MD et al. Polarized reflection removal with perfect alignment in the wild. In *Proceedings of the IEEE/CVF Conference on Computer Vision and Pattern Recognition* 1747–1755 (IEEE, 2020). https://doi.org/10.1109/CVPR42600.2020.00182.
33. Yao MD, Wang ML, Tam KM et al. PolarFree: polarization-based reflection-free imaging. In *Proceedings of the IEEE/CVF Conference on Computer Vision and Pattern Recognition* 10890–10899 (IEEE, 2025). https://doi.org/10.1109/CVPR52734.2025.01017.
34. Ulyanov D, Vedaldi A, Lempitsky V. Deep image prior. In *Proceedings of the IEEE/CVF Conference on Computer Vision and Pattern Recognition* 9446–9454 (IEEE, 2018). https://doi.org/10.1109/CVPR.2018.00984.
35. Garcia M, Davis T, Blair S et al. Bioinspired polarization imager with high dynamic range. *Optica* **5**, 1240–1246 (2018).
36. Kong N, Tai YW, Shin JS. A physically-based approach to reflection separation: from physical modeling to constrained optimization. *IEEE Trans Pattern Anal Mach Intell* **36**, 209–221 (2014).
37. Winthrop JT, Worthington CR. Theory of Fresnel images. I. Plane periodic objects in monochromatic light. *J Opt Soc Am* **55**, 373–381 (1965).
38. Zhang Q, He ZH, Xie ZW et al. Diffractive optical elements 75 years on: from micro-optics to metasurfaces. *Photonics Insights* **2**, R09 (2023).
39. Duan J, Liu J, Hao YF et al. Joint target geometry and polarization properties for polarization image fusion. *Opt Lasers Eng* **178**, 108176 (2024).
40. Dhariwal P, Nichol A. Diffusion models beat GANs on image synthesis. In *Proceedings of the 35th International Conference on Neural Information Processing Systems* 672 (Curran Associates Inc., 2021).
41. Ho J, Jain A, Abbeel P. Denoising diffusion probabilistic models. In *Proceedings of the 34th International Conference on Neural Information Processing Systems* 574 (Curran Associates Inc. , 2020).
42. Ronneberger O, Fischer P, Brox T. U-net: convolutional networks for biomedical image segmentation. In *Proceedings of the 18th International Conference on Medical Image Computing and Computer-Assisted Intervention* 234–241 (Springer, 2015). https://doi.org/10.1007/978-3-319-24574-4_28.
43. Wen Q, Tan YJ, Qin J et al. Single image reflection removal beyond linearity. In *Proceedings of the IEEE/CVF Conference on Computer Vision and Pattern Recognition* 3766–3774 (IEEE, 2019). https://doi.org/10.1109/CVPR.2019.00389.
44. Zhao H, Li MJ, Hu QM et al. Reversible decoupling network for single image reflection removal. In *Proceedings of the IEEE/CVF Conference on Computer Vision and Pattern Recognition* 26430–26439 (IEEE, 2025). https://doi.org/10.1109/CVPR52734.2025.02461.
45. Xiao K, Yates JM, Zardawi F et al. Characterising the variations in ethnic skin colours: a new calibrated data base for human skin. *Skin Res Technol* **23**, 21–29 (2017).
46. Ou FZ, Li CY, Wang SQ et al. CLIB-FIQA: face image quality assessment with confidence calibration. In *Proceedings of the IEEE/CVF Conference on Computer Vision and Pattern Recognition* 1694–1704 (IEEE, 2024). https://doi.org/10.1109/CVPR52733.2024.00167.
47. Boutros F, Fang ML, Klemt M et al. CR-FIQA: face image quality assessment by learning sample relative classifiability. In *Proceedings of the IEEE/CVF Conference on Computer Vision and Pattern Recognition* 5836–5845 (IEEE, 2023). https://doi.org/10.1109/CVPR52729.2023.00565.
48. Venables SV, Drerup C, Powell SB et al. Polarization vision mitigates visual noise from flickering light underwater. *Sci Adv* **8**, eabq2770 (2022).

Acknowledgements

National Natural Science Foundation of China (62441613).

Competing interests

The authors declare no competing financial interests.

Data availability

The code is publicly available at https://github.com/THUHoloLab/PDPrior.

Supplementary information

Supplementary information for this paper is available at https://doi.org/10.29026/oea.2026.250249

Open Access This article is licensed under a Creative Commons Attribution 4.0 International License, which permits use, sharing, adaptation, distribution and reproduction in any medium or format, as long as you give appropriate credit to the original author(s) and the source, provide a link to the Creative Commons license, and indicate if changes were made. To view a copy of this license, visit http://creativecommons.org/licenses/by/4.0/
©The Author(s) 2026.
Published by Editorial Office of *Opto-Electronic Advance*, Institute of Optics and Electronics, Chinese Academy of Sciences.

Opto-Electronic Journals Group
www.oejournal.org
Scan for Article PDF